Modeling of microwave-sustained plasmas at atmospheric pressure with application to discharge contraction

E. Castaños Martinez, Y. Kabouzi, K. Makasheva, and M. Moisan
Groupe de Physique des Plasmas, Université de Montréal, Montréal, Québec, Canada H3C 3J7
(Received 21 June 2004; published 17 December 2004)

The modeling of microwave-sustained discharges at atmospheric pressure is much less advanced than at reduced pressure (<10 Torr) because of the greater complexity of the mechanisms involved. In particular, discharge contraction, a characteristic feature of high-pressure discharges, is not well understood. To describe adequately this phenomenon, one needs to consider that the charged-particle balance in atmospheric-pressure discharges relies on the kinetics of molecular ions, including their dissociation through electron impact. Nonuniform gas heating plays a key role in the radial distribution of the density of molecular ions. The onset of contraction is shown to depend only on radially nonuniform gas heating. The radial nonuniformity of the electric field intensity also plays an important role allowing one, for instance, to explain the lower degree of contraction observed in microwave discharges compared to dc discharges. We present a numerical fluid-plasma model that aims to bring into relief the main features of discharge contraction in rare gases. It calls for surface-wave discharges because of their wide range of operating conditions, enabling a closer check between theory and experiment.

DOI: 10.1103/PhysRevE.70.066405 PACS number(s): 52.80.Pi, 52.25.−b

I. INTRODUCTION

Electrical discharges, whether they be dc or high-frequency (hf) discharges, are observed to undergo contraction when sustained at sufficiently high pressures (typically higher than 10 Torr in rare gases) [1–10]. The onset of contraction is found to depend also on the discharge power level, the discharge vessel, and the nature of the gas. This phenomenon can be observed with atomic and molecular gases, including electronegative gases. It is characterized by a local increase of both the electron density and the gas temperature and by a decrease of the electron temperature. In most cases, excepting the thermal arc discharge, the contracted plasma column is far from thermodynamic equilibrium [2,3]. In dc discharges in rare gases, in addition to the contraction phenomenon, one can also observe an abrupt transition from the diffuse state (uniform glow) of the discharge to the contracted state, this abrupt change in the plasma parameter values being characterized by a hysteresis in the current-voltage curve [4,5]. No such hysteresis is, however, observed in electronegative gas discharges [6]. Another specific effect related to contraction, this time observed with hf discharges only, is the breaking of a single plasma filament into two or more filaments of smaller diameters, which we refer to as filamentation [2,8,9]. It occurs when the field frequency and the radially averaged electron density are increased.

Several mechanisms have already been theoretically investigated to account for the radial contraction phenomenon [11–18]. Many of these studies focused on the abrupt transition, as a function of discharge current, from the diffuse to the contracted state in the positive column of dc discharges. More generally, two main mechanisms have been identified as playing a key role in the contraction process: (i) electron-electron collisions and (ii) nonuniform gas heating. Furthermore, for contraction to occur, it is generally accepted that charged-particle losses by volume recombination have to be dominant over those by ambipolar diffusion [11]. We briefly review the literature on these two main mechanisms.

Electron-electron collisions refill the tail of the electron energy distribution function (EEDF) depleted by inelastic collisions [19]. Provided the degree of ionization is large enough (typically $>10^{-4}$), further increasing electron-electron collisions can then turn the EEDF into a Maxwellian distribution. While this can be the case at the discharge axis, where the electron density is the highest, at the discharge periphery the EEDF could suffer from tail depletion, leading to a significant decrease of the ionization rate as one moves from the axis toward the wall. The effect of electron-electron collisions has been studied numerically in Refs. [17,18], with the conclusion that discharge contraction is due to the influence of electron-electron collisions on the ionization rate through their action on the EEDF. The second main mechanism invoked for contraction to occur is nonuniform gas heating along the discharge radius. Contraction of the discharge is indeed accompanied by a strong radial gradient of gas temperature since the temperature at the axis can be several hundred kelvin higher than at the tube wall. Nonuniform gas heating can be considered to be responsible for contraction in two ways. (1) It may occur through its influence on N, the density of atoms, and hence on the reduced electric field E/N [11–13]. Then, since the value of E/N decreases from the axis toward the tube wall (E is constant in dc discharges), there results a rapid decrease of the ionization frequency, which is a sensitive function of the reduced electric field. (2) It may occur through the influence of the gas temperature on the density of molecular ions [14,15]. Because of the radial gradient of the gas temperature, the density of molecular ions increases from the axis toward the wall, leading to a rapid increase of charged-particle losses through dissociative recombination. This is because, at the discharge axis, the gas temperature is high enough that molecular ions are efficiently dissociated via atomic collisions, therefore reducing

the number of molecular ions available for charged-particle losses through dissociative recombination.

Although the above mechanisms have been included in the theoretical models, satisfactory interpretation of the contraction phenomenon is still lacking since, in particular, none of these studies clearly shows which of the two main mechanisms mentioned is at the origin of the radial contraction. In Refs. [16–18], radial contraction has been interpreted as a direct consequence of electron-electron collisions and of their correlative effect on the EEDF. This is because, when ignoring electron-electron collisions in the modeling, a continuous, and not abrupt, contraction of the density profile of the positive column is obtained with increasing current, whereas experiments show an abrupt change in the plasma parameters and a corresponding hysteresis as current is increased. This modeling result led these authors to conclude that nonuniform gas heating was not playing a primary role. We surmise that this chain of reasoning is partly wrong. To see this, consider, for example, Refs. [16–18], where both experimental and modeling results clearly show that the onset of radial contraction and the abrupt jump in the plasma parameters are taking place at different current values. For instance, in argon discharges sustained at 100 Torr, radial contraction sets in at a current value of 4 mA, whereas the abrupt jump in the plasma parameters is observed for a current value of 10 mA. Therefore, we believe that the abrupt jump in the plasma parameters is, in fact, due to the increase of electron-electron collisions, but that this mechanism is not a determining factor for the onset of contraction. Another feature not explained by the effect of electron-electron collisions is the observed increase of the discharge radius, i.e., a reduction of the contraction degree as the discharge current is increased [4,14,15].

The intent of this work is to bring some more insight into the mechanism of radial contraction and, in particular, to show how nonuniform gas heating induces radial contraction through its effect on molecular ion kinetics. Therefore, one needs to describe adequately all the relevant kinetic processes related to the creation and losses of molecular ions. As we will show, even though the density of molecular ions is lower than that of atomic ions in the case of rare-gas discharges, the molecular ions actually control the ionization-recombination kinetics. The previous models [14,15] that took into account molecular ions supposed them to be in equilibrium with atomic ions through heavy-particle collisions, ignoring the importance of their dissociation by electron collisions. As a matter of fact, the kinetic processes involving molecular ions determines a gas temperature range over which contraction can be observed, corresponding to discharges in the electron density range 10^{12}–10^{15} cm^{-3}.

The model considered in the present study refers to a microwave discharge sustained in argon at atmospheric pressure. More specifically, the discharge is sustained by an electromagnetic surface wave [20–25]. This type of discharge not only yields the largest possible range of operating conditions in terms of gas pressure, field frequency, and tube diameter, but also provides a continuous variation as a function of axial position of the electron density. To account for stepwise ionization but, nonetheless, to keep the model simple and transparent, we limit ourselves to the first excited configuration of argon. It provides the main characteristics of the ionization-recombination processes required to bring out the essential phenomena. Another original feature of the model is to take into account the radial variation of the electric field intensity.

The article is organized as follows. Section II describes the plasma equations on which our model is based. The influence of molecular ion kinetics and of nonuniform gas heating on the discharge radial contraction is emphasized. Section III presents the field equations necessary to complete the set of plasma equations for a self-consistent treatment of the discharge contraction in the particular case of microwave discharges. Our results are discussed in Sec. IV. Finally, concluding remarks are presented in Sec. V.

II. PLASMA EQUATIONS

We consider a long argon-plasma column sustained in a dielectric tube with internal and external radii R and R_1, respectively. The discharge is stationary and maintained at atmospheric gas pressure. These conditions correspond to charged-particle losses dominated by volume recombination. A two-temperature fluid model [24,26] is used to describe the radially contracted argon discharge. In this approximation, the plasma is considered to comprise two main species: the electrons and the heavy particles. Maxwellian energy distribution functions characterized by temperatures T_e and T_g are assumed for electrons and heavy particles, respectively. The heavy particles are argon atoms (ground state and excited states) and ion species. Two types of ions are considered in this model, namely, atomic ions with density n_{i1} and molecular ions with density n_{i2}. Quasineutrality of the charged particles is assumed, i.e., $n_e = n_{i1} + n_{i2}$, where n_e is the density of electrons.

A. Energy balance equation for heavy particles

As shown by experiments [9], at atmospheric pressure, the discharge gas is strongly heated, inducing a steep radial gradient of gas temperature. To account for the influence of nonuniform gas heating on the plasma parameters and determine T_g, we use the gas energy balance equation. This equation reads

$$-\nabla \cdot (\chi_g \nabla T_g) = \frac{3}{2} n_e \delta \nu k_B (T_e - T_g), \tag{1}$$

where χ_g is the gas thermal conductivity, $\delta = 2m_e/M$ (where m_e and M are the electron and atom masses, respectively) is the energy transfer coefficient for elastic collisions, ν is the elastic collision frequency and k_B is the Boltzmann constant. The heavy particles are being heated by electrons through elastic collisions. This energy is in the end lost to the tube walls through thermal conduction of the gas. The imposed boundary conditions for the heavy-particle balance equation are

$$\left.\frac{dT_g}{dr}\right|_{r=0} = 0, \quad T_g(r = R) = 900 \text{ K}, \tag{2}$$

and the value of the gas temperature at the tube wall is set according to experimental data [9].

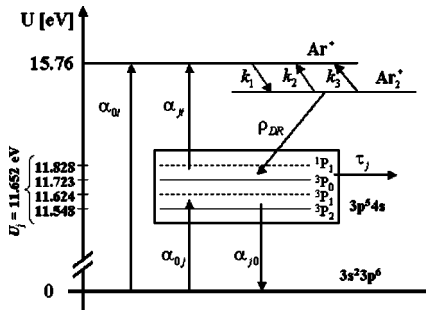

FIG. 1. Schematic diagram of the energy levels of the argon atom considered in the model. The arrows indicate the collisional and transport processes taken into account in the balance equations of the charged particles.

B. Energy balance equation for electrons

The electron temperature T_e is obtained as a solution of the electron energy balance equation, written in the following form:

$$-\nabla\cdot(\chi_e\nabla T_e)+\frac{3}{2}n_e\delta\nu k_B(T_e-T_g)+\frac{3}{2}n_e\nu_* k_B U_*=\sigma_r|E|^2, \tag{3}$$

where σ_r is the real part of the plasma conductivity, E is the electric field intensity, ν_* is the frequency of inelastic collisions for total excitation, U_* is the energy of the first excited state of the atom ($U_*=11.548$ eV for argon), and χ_e is the electron thermal conductivity. The electron energy losses through thermal conductivity and through collisions (elastic collisions and inelastic collisions) are compensated by the Joule heating of the applied field, $\sigma_r|E|^2$. The boundary conditions for the electron temperature equation are

$$\left.\frac{dT_e}{dr}\right|_{r=0}=\left.\frac{dT_e}{dr}\right|_{r=R}=0. \tag{4}$$

The boundary condition at the tube wall assumes that the electrons are reflected by the electric field within the sheath near the tube wall (adiabatic condition) [24,26].

C. Charged-particle balance equations

Three types of charged particles are taken into account, namely, electrons, atomic ions (AIs), and molecular ions (MIs), by writing the continuity equation for each type of charged particle. In each equation, the contribution to ambipolar diffusion is specific to the kind of charged particles under consideration. The processes of creation and losses of charged particles, necessary to complete the balance equations, are determined following the energy diagram given in Fig. 1. A three-level energy scheme is used—the ground state, the first excited configuration of the rare gas, and the ionization level. Such a simplification of the kinetic picture enables us to keep the model simple while, nonetheless, providing the main characteristics of the discharge. The first excited configuration of the argon atom is comprised of two metastable states $^3P_2$ and $^3P_0$, and two radiative states $^3P_1$ and $^1P_1$, which are considered as a block, designated 4*s*, with a mean energy of the block $U_j=11.652$ eV [27]. The 4*s* block is populated by electron collisions on the ground state atom and also through dissociative recombination [28]. It is depopulated through diffusion, collisional transition to the ground state, and ionization. Radiation from the $^3P_1$ and $^1P_1$ resonant states is not considered because of the corresponding high optical thickness of the plasma. The three-level system just described is coupled to the molecular ions through collisional processes [29]. These are the conversion of atomic ions into molecular ions, the dissociation of molecular ions by electron and atom impacts, and dissociative recombination. The rate coefficients of all the collisional processes considered in the model are obtained after integration of the corresponding cross sections over a Maxwellian electron velocity distribution. The expressions of these rate coefficients as well as those characterizing the transport processes in the discharge are given in the Appendix. In this way, the electron-density balance equation reads

$$\nabla\cdot\left[\frac{D_e}{b_e}\left(b_{i1}\frac{n_{i1}}{n_e}+b_{i2}\frac{n_{i2}}{n_e}\right)\nabla n_e\right]+\nu_i n_e+\frac{\rho_{si}n_e^2+\rho_{rk}n_{i2}n_e^2}{1+\eta n_e}-\rho_{dr}n_{i2}n_e-\rho_{tr}n_{i1}n_e^2=0, \tag{5}$$

with boundary conditions

$$\left.\frac{dn_e}{dr}\right|_{r=0}=\left.\frac{dn_e}{dr}\right|_{r=R}=0. \tag{6}$$

The boundary condition for n_e at the tube wall is inferred from the boundary condition of the electron temperature at the same radial position [30]. The losses of electrons are due to ambipolar diffusion (first term on the left hand side), volume recombination, including dissociative recombination (with coefficient ρ_{dr}), and three-body recombination (with coefficient ρ_{tr}). These particle losses are compensated by the creation of electrons due to direct ionization on the ground level (with frequency ν_i) and through step ionization from the 4*s* block. In Eq. (5), in the step-ionization term, the rate coefficient ρ_{si} accounts for step ionization through states initially excited from the ground level while ρ_{rk} takes into account step ionization stemming from states populated by dissociative recombination. The coefficient η accounts for the saturation of the various step-ionization processes. In expression (5) above, D_e and b_e are the coefficients of diffusion and mobility of electrons while b_{i1} and b_{i2} are the mobility coefficients of atomic and molecular ions, respectively.

The continuity equation for AIs reads

$$\nabla\cdot(D_{A(i1)}\nabla n_{i1})+\nu_i n_e+\frac{\rho_{si}n_e^2+\rho_{rk}n_{i2}n_e^2}{1+\eta n_e}+k_2n_{i2}n_e+k_3n_{i2}N-k_1n_{i1}N^2-\rho_{tr}n_{i1}n_e^2=0. \tag{7}$$

The AIs are provided by direct ionization, step ionization, dissociation of MIs by electron impact (with rate coefficient k_2), and atom impact (with rate coefficient k_3). Their losses result from ambipolar diffusion [with coefficient $D_{A(i1)}=D_e(b_{i1}/b_e)$], from their conversion into MIs (with rate coefficient k_1), and the three-body recombination.

The continuity equation for MIs reads

$$\nabla \cdot (D_{A(i2)} \nabla n_{i2}) + k_1 n_{i1} N^2 - \rho_{dr} n_{i2} n_e - k_2 n_{i2} n_e - k_3 n_{i2} N = 0, \tag{8}$$

where the second term represents the process of conversion of atomic ions into molecular ions (at high gas pressure, this is the main creation channel for MIs and the only one taken into account in the model). The losses of MIs are due to ambipolar diffusion [with coefficient $D_{A(i2)}=D_e(b_{i2}/b_e)$], dissociative recombination, and dissociation of the molecular ions by electron and atom impacts.

The atom density N is obtained from Dalton's law:

$$N = \frac{p}{k_B T_g} - n_e\left(1 + \frac{T_e}{T_g}\right), \tag{9}$$

where p is the gas pressure.

D. Role of the MIs and of the gas temperature in discharge contraction

1. Influence of molecular ions over the process of step ionization

The presence of MIs in rare-gas discharges strongly influences both the creation and losses of charged particles. As the gas pressure is increased ($p \geqslant 1$ Torr, in argon discharges), volume dissociative recombination becomes dominant over ambipolar diffusion as far as charged-particle losses are concerned [31,32]. Dissociative recombination can also influence charged-particle creation, since in rare-gas discharges, one of the two resulting atoms is in an excited state, therefore enhancing the process of step ionization, as accounted for in Eq. (5). Because of this, the step-ionization frequency depends not only on the electron density but also on the MI density. When the step-ionization process saturates with increasing electron density, i.e., when its ionization frequency no longer depends on electron density, it nonetheless keeps on depending on the density of charged particles through MI density. Such a dependence is actually one of the conditions for contraction to develop. At low gas pressure, for instance, $p=1$ Torr, the second term of the contribution to the step-ionization rate ($\rho_{rk} n_{i2} n_e^2 = 5.03 \times 10^{14}$ cm^{-3}/s) is negligible, actually three orders of magnitude lower than the first one ($\rho_{si} n_e^2 = 7.61 \times 10^{17}$ cm^{-3}/s). As gas pressure is increased, the contribution of the second term becomes more and more important and, at atmospheric pressure, it is four times larger ($\rho_{rk} n_{i2} n_e^2 = 2.04 \times 10^{22}$ cm^{-3}/s) than the first one ($\rho_{si} n_e^2 = 5.11 \times 10^{21}$ cm^{-3}/s) [33].

2. Influence of the gas temperature on the density of charged particles

To determine the influence of nonuniform gas heating on the discharge radial contraction, we consider the dependence of the charged-particle densities on the gas temperature T_g as obtained from Eqs. (5)–(9). Figure 2 shows the variation of the electron, atomic, and molecular ion densities as functions of T_g, in an argon discharge at atmospheric pressure with $T_e = 10\,500$ K and $R=3$ mm. The electron density increases by more than an order of magnitude when T_g increases from 1500 to 2500 K, while the molecular ion density remains almost constant. The atomic ion density increases by more than three orders of magnitude over the 500 to 3500 K temperature range. This strong variation of the AI density with T_g is induced by atom-impact dissociation of MIs, the rate coefficient of which depends exponentially on T_g (see the Appendix).

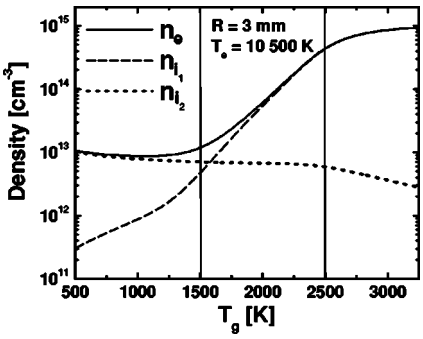

FIG. 2. Electron density n_e (full curve), atomic ion density n_{i1} (dashed curve), and molecular ion density n_{i2} (dotted curve) as functions of the gas temperature T_g at a fixed value of the electron temperature T_e.

To examine in detail the dependence of the charged-particle densities on T_g, we divide the gas temperature range in Fig. 2 into three regions: region I for $T_g < 1500$ K, region II for $1500 < T_g < 2500$ K, and region III for $T_g > 2500$ K. In region I, the electron density decreases slightly because of the decrease of the frequencies of direct and step ionization with increasing T_g and hence decreasing N. For the same reason, the MI density decreases in accordance with the decrease of the conversion of AIs into MIs. The AI density increases very fast due to the increasing contribution with T_g of the dissociation of MIs via atom impact. Nonetheless, as far as the charged-particle balance is concerned, the dissociation of MIs by atom impact is negligible in this region. In region II, the electron and atomic ion densities increase while the molecular ion density stays approximately constant. The fast increase of the AI density, in this region, is due to the strong (exponential) dependence of the atom-impact dissociation of MIs on T_g. As far as the interaction of electrons with MIs is concerned, the dissociation of the MIs is then more probable than the dissociative recombination process, and hence there is a lower loss rate of charged particles. In addition, although the density of atomic ions is greatly increased, the loss of charged particles through three-body recombination is negligible in this region. In region III, the electron and AI densities reach a plateau because of the increasing importance of the three-body recombination process at higher electron density. The MI density decreases in this region, since the conversion of atomic ions into molecular ions decreases. This is due to the saturation of the AI density (owing to three-body recombination) and, at the same time, to the atom-impact dissociation of MIs that keeps on increasing. Nevertheless, even with such a low MI density (MI density is more than two orders of magnitude lower than AI density), electron losses are still controlled by dissociative recombination because its frequency (3.5×10^4 s^{-1}) is three times higher than the three-body recombination frequency (1.2×10^4 s^{-1}) at $T_g = 3500$ K.

Finally, Fig. 2 clearly shows that, even at constant electron temperature, the electron density can vary by more than an order of magnitude as a consequence of a gas temperature variation. This is the case in a contracted discharge where the gas temperature decreases strongly from the axis toward the tube wall.

III. SURFACE-WAVE FIELD EQUATIONS

The discharge characteristics are strongly influenced by the way that the electric field energy is transferred to the plasma. Therefore, a full description of the discharge properties requires completing the plasma equations with those describing the applied electric field, i.e., the term in the right hand side of Eq. (3) has to be specified. While in the case of dc discharges, this term is connected to the current density, in the case of wave-sustained discharges, it represents the Joule heating in the wave electric field and implies knowing the wave propagation characteristics. One of the reasons for considering a gas discharge sustained by a propagating electromagnetic surface wave for modeling microwave discharges is the fully self-consistent coupling existing between the electromagnetic field and the plasma [20,21,24,25,31]: the wave properties depend on the plasma properties and conversely. Another reason for using surface-wave-sustained discharges (SWDs) is their flexibility in terms of operating conditions, making them the most suitable for parametric studies. A further reason is that in SWDs the absorbed wave power decreases away from the wave launcher along the plasma column, making the plasma medium varying continuously. This provides a useful way to investigate different stages of discharge contraction and to more closely compare theoretical results with available experimental data.

In this model, the plasma column is sustained by a propagating azimuthally symmetric surface wave (SW) (a TM mode with nonzero wave field components E_r, H_φ, E_z and a field variation of a form proportional to $\exp[-i\omega t + i\int_z k(z)dz]$ where ω is the wave angular frequency, $k=\beta + i\alpha$ is the complex wave number with β and α being the wave number and the space damping rate, respectively, and z is the axial coordinate). The waveguiding structure consists of the plasma, the dielectric tube (with internal and external radii R and R_1, respectively, and glass permittivity ε_d) and the surrounding vacuum.

The wave loses its energy as it propagates and the amount of wave power that is lost over a unit axial length for sustaining the discharge is

$$L(z) = 2\pi \int_0^R r\sigma_r |E(r,z)|^2 dr, \tag{10}$$

where $\sigma_r(r,z)=\varepsilon_0 \nu(r,z)[n_e(r,z)/n_{cr}]\{1+[\nu(r,z)/\omega]^2\}^{-1}$ is the real part of the plasma conductivity [$n_{cr}=\varepsilon_0 m\omega^2/e^2$ is the critical density, ε_0 is the vacuum permittivity, and e and m_e are the electron charge and mass, respectively]. Equation (10) relates the wave characteristics with the plasma properties through Joule heating. The wave power lost within the axial interval z, $z+dz$, as expressed by $L(z)$, is absorbed in the plasma column over that same axial interval: self-consistency between the wave and the plasma is local. It implies that we are assuming the plasma column to be locally axially uniform, i.e., we neglect the presence of axial gradients in the plasma slab considered.

Introducing $L(z)$ into the local wave energy balance equation enables us to obtain the plasma parameters at each axial position. This is because the plasma parameters at a position z are uniquely related to $L(z)$ [21,23,24]. The local wave energy balance equation reads

$$\frac{dP(z)}{dz} \equiv -2\alpha P(z) = -L(z), \tag{11}$$

where dP/dz is the amount of power lost by the wave while $L(z)$ is the power absorbed in the plasma column, $P(z)$ is the wave power flux, and α is the space damping rate (attenuation coefficient) of the wave. The attenuation and propagation coefficients α and β are derived from the local (in the z direction) wave dispersion relation

$$D[\omega, k(z) = \beta(z) + i\alpha(z), \varepsilon(r,z), \varepsilon_d, R, R_1] = 0. \tag{12}$$

Here $\varepsilon(r,z)=1-[n_e(r,z)/n_{cr}]\{1+i[\nu(r,z)/\omega]\}^{-1}$ is the plasma permittivity for a collisional and radially inhomogeneous plasma. The radial distribution $\nu(r,z)$ of the elastic collision frequency and the radial distribution $n_e(r,z)$ of electron density stem from the plasma equations (Sec. II). The dispersion relation is solved after applying the continuity conditions of the E_z and H_φ electric field components at the interfaces ($r=R,R_1$). The electric field components are obtained from the wave equation

$$\frac{d^2E_z}{dr^2} + \left[\frac{1}{r} + \frac{k^2}{\kappa_p^2(\omega,r)\varepsilon(\omega,r)}\frac{d\varepsilon(\omega,r)}{dr}\right]\frac{dE_z}{dr} - \kappa_p^2(\omega,r)E_z = 0, \tag{13a}$$

$$E_r = -i\frac{k}{\kappa_p^2(\omega,r)}\frac{dE_z}{dr}, \tag{13b}$$

where $\kappa_p^2(\omega,r)=k^2-[\omega^2\varepsilon(\omega,r)/c^2]$ characterizes the electric field distribution in the plasma region $r\leqslant R$ (radially inhomogeneous collisional plasma) and, with $\varepsilon(\omega,r)$ replaced by ε_d or 1, in the dielectric ($R\leqslant r\leqslant R_1$) and vacuum ($r>R_1$) regions, respectively. In this model, the radial variation of the elastic collision frequency $\nu(r,z)$ needs to be taken into account in the calculations since its influence over the electric field radial variation, as we will show, is important.

IV. RESULTS AND DISCUSSION

The numerical calculations of the plasmas parameters, namely, T_e, T_g, n_e, n_{i1}, n_{i2}, and ν and the wave characteristics E, α, and β, are performed for given discharge conditions and a set of successive values of the linear power density L. The results presented in this section have been computed for a surface-wave argon discharge sustained in a fused silica tube ($R=3$ mm internal radius and $R_1=4$ mm external radius with permittivity $\varepsilon_d=3.78$) at $f=\omega/2\pi=915$ MHz, and at atmospheric pressure.

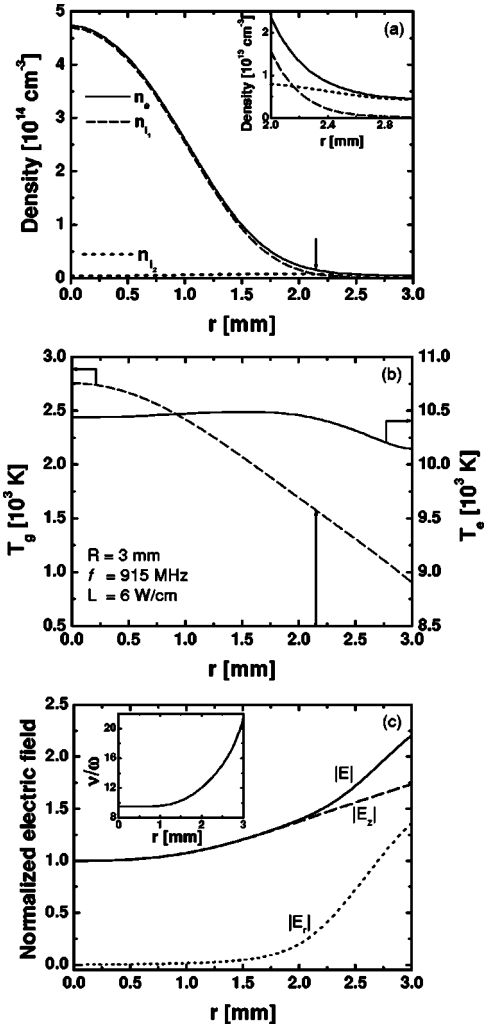

FIG. 3. (a) Radial distributions of n_e (full curve), n_{i1} (dashed curve), and n_{i2} (dotted curve). The arrow shows the radial position at which the atomic-ion (AI) density becomes larger than the molecular-ion (MI) density as r decreases. The inset is a magnified view of the radial variation of the charged-particle densities close to the discharge wall. (b) Radial distributions of the gas temperature T_g (dashed curve) and electron temperature T_e (full curve). The vertical arrow shows the radial position corresponding to the value of the gas temperature at which the AI density becomes larger than the MI density as r decreases. (c) Radial profiles in the plasma region of the radial $|E_r|$ (dotted curve) and axial $|E_z|$ (dashed curve) components of the electric field intensity and of the total electric field intensity (full curve) [all normalized to $|E_z(r=0)|$]. The inset shows the radial variation of ν/ω. Calculations made for $f=915$ MHz, $R=3$ mm, and $L=6$ W/cm.

A. Radial distribution of the plasma parameters and wave field components

Figures 3(a)–3(c) show results for the radial distribution of the plasma parameters and the radial profile of the electric field intensity components [normalized to $|E_z(r=0)|$], as obtained self-consistently from the model for a fixed value of power density $L=6$ W/cm. Figure 3(a) shows that the argon discharge does not fill the discharge tube ($R=3$ mm), i.e., it is contracted: The electron density falls by two orders of magnitude from the axis toward the tube wall. Actually, n_e decreases from 4.7×10^{14} cm^{-3} at the discharge axis to 4.5×10^{12} cm^{-3} at the wall. The radial distributions of AI and MI densities are also shown in Fig. 3(a). Ar^+ is the dominant ion over the discharge cross section, except in the region close to the tube wall. The strong increase of the electron density starts at the radial position [indicated by arrows in Figs. 3(a) and 3(b)] where the gas temperature exceeds some value (approximately 1500 K in the present case), in accordance with the explanations provided with Fig. 2. This radial position corresponds to the radial position at which the AI density exceeds the MI density [see inset in Fig. 3(a)]. This shows that the contraction is initiated by the nonuniform heating of the discharge gas. As can be seen in Fig. 3(b), the electron temperature is several times higher than the gas temperature everywhere within the discharge volume and varies slowly over the discharge cross section. The shift of the maximum of T_e toward the tube wall is due to the increase of the electric field intensity toward the tube wall [see Fig. 3(c)]. In contrast, the gas temperature is the highest at the axis and decreases rapidly toward the wall.

Figure 3(c) shows the radial profiles of the electric field intensity components in the plasma. In the fused silica tube and vacuum regions [not shown in Fig. 3(c)], the field components are well known and can be represented using a combination of Bessel functions [22,31,34,35]. The strong radial inhomogeneity of the electric field intensity is caused by the steep radial variation of both the electron density and the elastic collision frequency. The radial variation of the elastic collision frequency (ν/ω increases by more than twice towards the discharge wall [inset in Fig. 3(c)]) acts in an opposite way on the axial $|E_z|$ and on the radial $|E_r|$ components of the electric field intensity. The gradient of $|E_z|$ decreases while $|E_r|$ strongly increases as the gradient of ν/ω increases, in the end increasing the gradient of the total field intensity [Fig. 3(c)]. Therefore, even though the plasma is highly collisional, we observe that the radial increase toward the wall of the ν/ω ratio enhances the inhomogeneity of the total electric field intensity.

B. Influence of the linear power density

Figures 4(a)–4(d) show the radial distribution of the plasma parameters and the radial profile of the electric field intensity for successive values of the linear power density L (increasing values of L correspond to increasing values of axial position z, $z=0$ being the end of the plasma column). Figure 4(a) shows that the electron density profile expands with increasing L, that is the discharge radial contraction reduces with increasing L. The maximum of electron density shifts radially towards the wall at high enough values ($L\geqslant16$ W/cm) of the power density. These features of SWDs at atmospheric pressure have already been observed experimentally [9]. The shift in the maximum value of n_e toward the wall is due to a smaller penetration of the electric field intensity in the plasma volume, because the average electron density increases, as power density is increased.

As shown in Fig. 4(b), the gas temperature increases significantly with increasing L and the region over which the

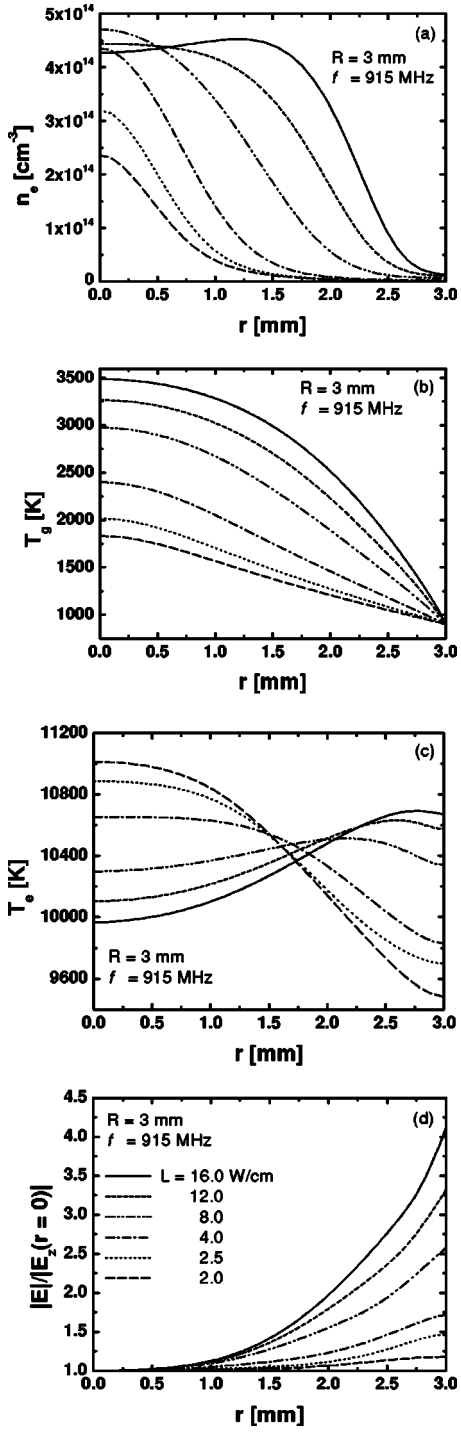

FIG. 4. Radial distributions of (a) the electron density, (b) gas temperature, (c) electron temperature, and (d) the radial profile of the total electric field intensity at successive values of the linear power density.

gas is heated is enlarged. In contrast, the electron temperature depends slightly on L, as shown in Fig. 4(c). The radial distribution of T_e is mainly determined by the radial profile of the electric field intensity. Actually, at low values of L (2–4 W/cm), the inhomogeneity of the electric field intensity is small and T_e has its maximum value at the axis and decreases toward the tube wall. At high enough values of L,

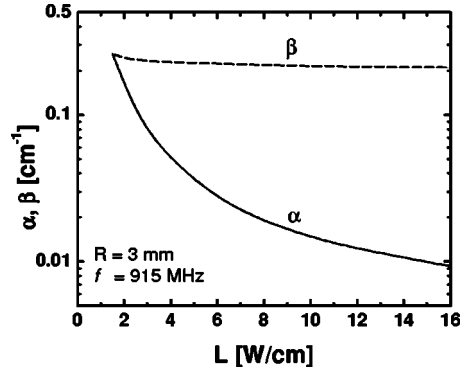

FIG. 5. Wave number β and space damping rate α as functions of the linear power density L.

the electric field intensity strongly increases toward the tube wall, leading to an increase of T_e close to the tube wall and its decrease near the axis. These changes in the radial profile of the electron temperature affect the radial profile of the electron density, finally leading to the density profile shown in Fig. 4(a) at $L=16$ W/cm. From the above, we conclude that an increasing radial inhomogeneity of the electric field intensity reduces the radial contraction of microwave discharges. However, a further increase of the inhomogeneity of the electric field intensity can result in the filamentation of the discharge. In Refs. [36,37], the filamentation of SWDs is theoretically studied at reduced gas pressure ($p>10$ Torr), concluding that the onset of filamentation depends on the gas temperature.

C. Axial structure of the discharge

In the previous section, we have obtained, self-consistently, the radial distribution of the plasma parameters and of the wave characteristics for given values of $L(z)$, i.e., for corresponding plasma slabs z, $z+dz$, which amounts to assuming these slabs to be axially uniform. In this local uniformity approximation [21,23–25,31], we consider that all the axial gradients of the plasma parameters are small in comparison with their corresponding radial gradients. In this case, the plasma parameters and the wave propagation characteristics rely only on the imposed discharge operating conditions (tube radius, pressure, and field frequency) and on the local value of the power L dissipated per unit length. Therefore, we can express the attenuation and propagation coefficients of the wave directly as functions of the power density L.

Figure 5 presents $\alpha(L)$ and $\beta(L)$, as obtained self-consistently (the plasma parameters and the wave characteristics are determined simultaneously) from the model assuming the local uniformity approximation (see Sec. IV B). The wave can propagate only when $\alpha<\beta$. As a practical criterion in the model, the end of the plasma column is taken as the position at which $\alpha\cong\beta$, which corresponds in the present case to $L=1.5$ W/cm. Figure 5 shows that β is almost independent of L whereas α decreases monotonically with L. Having now in hand the functional $\alpha(L)$, we can obtain the axial structure of the discharge using Eq. (11).

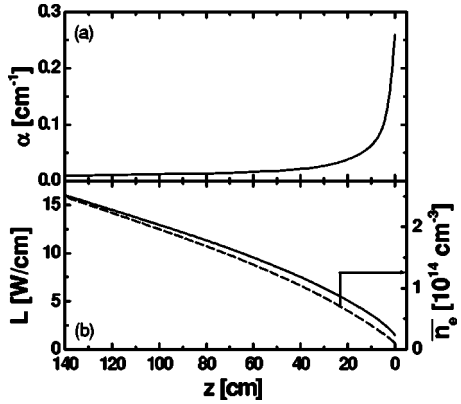

FIG. 6. Axial variation of (a) the space damping rate $\alpha(z)$, (b) the axial variations of the linear power density $L(z)$ and the average electron density $\overline{n_e}(z)$. The axial position $z=0$ corresponds to the end of the plasma column.

Figure 6 shows the calculated axial distribution of the wave-attenuation coefficient $\alpha(z)$, the linear power density $L(z)$, and the electron density averaged over the tube cross section $\overline{n_e}(z)$. As expected in the case of a discharge sustained by a traveling wave [23,31], both $L(z)$ and $\overline{n_e}(z)$ decrease toward the end of the plasma column ($z=0$). At high enough electron density values, the attenuation coefficient is constant while it increases rapidly toward the very end of the column as the electron density decreases. The column ends when $\alpha \cong \beta$, as shown in Fig. 5.

D. Comparison of the contraction phenomenon in SW and dc discharges

In addition to the radial contraction, which is common to both hf and dc discharges, the former discharges are observed to suffer filamentation [8–10]. Filamentation is related to the limited penetration of the hf electric field in the plasma volume, commonly known as the electromagnetic skin effect. In this section, we further examine the influence of the radial inhomogeneity of the electric field intensity on contraction as encountered in surface-wave discharges compared to the case of dc discharges where the electric field intensity is uniform.

Figures 7(a) and 7(b) compare the radial profiles of $T_e(r)$ and $n_e(r)$, normalized to their values at the discharge axis, for both types of discharge. The results are for the same and successive values of L at $R=3$ mm. We note from Figs. 7(a) and 7(b) that for the lowest value of the absorbed power density $L=4$ W/cm—which corresponds to the end of the plasma column in case of a SWD and to a discharge current $I \cong 0.5$ A in the case of a dc discharge—both discharges exhibit the same radial electron density profile. The value of the electron density at the discharge axis (not shown) is, however, higher in the case of dc discharge for the same amount of absorbed power density. The electron temperature profiles are also almost the same for both types of discharge, except close to the tube wall where, for the SWD, T_e exhibits a weaker radial decrease (due to the radial inhomogeneity of the electric field intensity). Actually, in both cases, the electron density profile is determined by the radial gradient of gas temperature [which presents the same radial variation for both dc and SWDs; the case of SWDs is shown in Fig. 4(b)]. When increasing the absorbed power density ($L=12$–16 W/cm), the difference between SWD and dc discharges becomes significant. In both discharges, the electron density profile expands with increasing L, i.e., the discharge radial contraction lowers with increasing L. For the dc discharge, the radial profile of T_e is observed to be slightly dependent on L and the electron density profile keeps the same radial variation with increasing L: it monotonically decreases from the discharge axis toward the tube wall. For the surface-wave discharge, the value of the electron temperature is observed to be almost independent of L [see Fig 4(c)] but its profile is very sensitive to the radial variation of the electric field intensity. In SWDs, in contrast to dc discharges, the shape of the electron density radial profile changes at large enough L values, the radial position of the electron density maximum being shifted from the axis toward the tube wall. This results in a much less contracted discharge in the case of SWDs compared to the dc discharges, at the same amount of absorbed power density. For instance, to obtain an equivalent discharge radius, the absorbed power density for the dc discharge has to be approximately twice the value of the power density in SWD ($L=12$ W/cm), which corresponds to an increase of the current from 2.7 to 5.2 A.

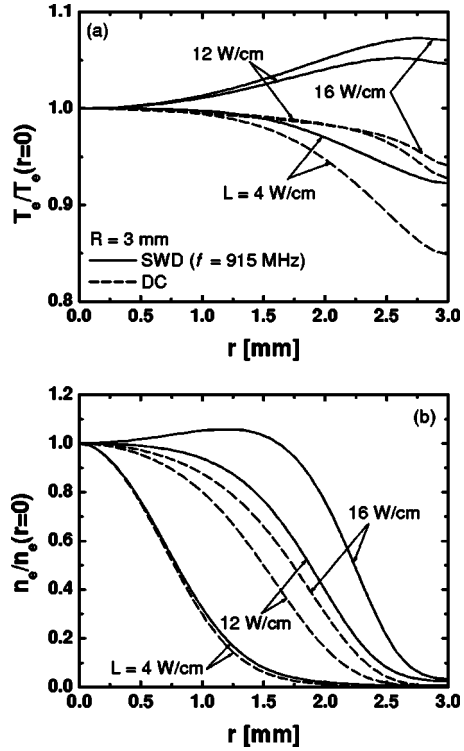

FIG. 7. Radial profiles of (a) the electron temperature and (b) the electron density, at three values of the absorbed power density, for a surface-wave discharge (SWD) and a direct-current (dc) discharge.

E. Comparison between theoretical and experimental results

Optical emission spectroscopy was employed to determine the electron density and the plasma radius of an argon

surface-wave discharge sustained at atmospheric pressure at an applied field frequency $f=915$ MHz and in a fused silica tube with $R=3$ mm.

Because of contraction, the plasma radius is too small to obtain the electron density radial distribution, which would require determining the radial variation of the $\lambda=486.13$ nm H_β line broadening through Abel inversion. Instead, we have determined the average electron density. This was achieved by determining (1) the radial profile of the electron density, assuming that it is reflected by the radial profile of the H_β line emission intensity, as obtained through Abel inversion; (2) the electron density at the discharge axis along the argon plasma column, using the Stark broadening of the H_β line [9]. Then, the average electron density is determined using the following expression:

$$\overline{n_e}(z) = \frac{n_e(r=0)}{\pi R^2} \int_0^R I_{H_\beta}(r,z) 2\pi r \, dr, \tag{14}$$

where $n_e(r=0)$ is the measured electron density at the axis and $I_{H_\beta}(r,z)$ is the obtained radial profile of the H_β line emission intensity. The average electron density determined from the model is directly calculated by integrating the electron density radial distribution over the discharge tube cross section:

$$\overline{n_e}(z) = \frac{2}{R^2} \int_0^R r n_e(r,z) dr. \tag{15}$$

The plasma radius (R_p) is obtained experimentally from the full width at half maximum of the radial profile of the H_β line emission intensity, while from the model, R_p is determined as the full width at half-maximum of the electron density radial profile.

In Fig. 8, we compare the results from the model with the experimental data. Figure 8(a) shows that there is a good agreement between the calculated and the measured axial distribution of the average electron density. A similar agreement is observed between the calculated and measured plasma radius along the column [see Fig. 8(b)]. In both cases, the experimental values are slightly higher than the calculated ones: they differ by a factor 1.5–2. A possible reason for such a deviation of the average electron density could be the simplified kinetic scheme used in the model for the excitation and ionization processes. Other possible reasons are (i) the neglect of the axial gas flow in the model; its effect on the energy balance could be important, since the tube diameter is small ($2R=6$ mm) and the gas flow rate is relatively high (0.5 standard liter per minute): (ii) the assumed value of the gas temperature at the wall $[T_g(r=R)=900\ \mathrm{K}]$ in the modeling.

The above results show that the present model correctly predicts the observed experimental trends even though the radial variation of the EEDF due to the effect of electron-electron collisions has been neglected in the calculations. Actually, the assumption of a Maxwellian EEDF at atmospheric pressure is sound. To support this assumption, we have estimated the various channels for electron energy losses relevant to the behavior of the EEDF, namely, elastic

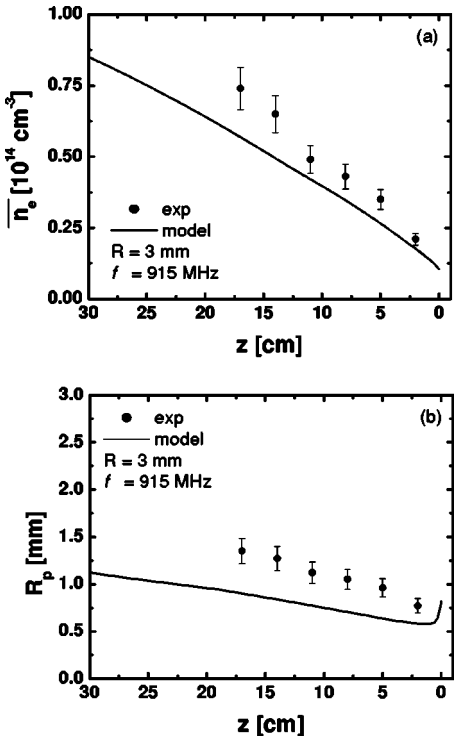

FIG. 8. Calculated and measured axial distributions of (a) the average electron density $\overline{n_e}(z)$ and (b) the plasma column radius $R_p(z)$.

collisions with heavy particles for momentum transfer $\delta\nu$ and inelastic collisions for excitation ν_*, and compared them to the electron-electron collision frequency ν_{ee}. We have found that

$$\nu_{ee} \gg \delta\nu > \nu_*. \tag{16}$$

For instance, at the discharge axis the frequency of electron-electron collisions ($\nu_{ee}=1.8\times10^{10}\ \mathrm{s}^{-1}$) is four orders of magnitude higher than the frequency of elastic collisions between electrons and heavy particles ($\delta\nu=1.5\times10^{6}\ \mathrm{s}^{-1}$); close to the wall, ν_{ee} is almost two orders of magnitude higher than $\delta\nu$. According to Ref. [41], inequality (16) assures the Maxwellization of the EEDF, at least within its bulk. As for its tail, because of the strong energy loss in excitation collisions, it could deviate from a Maxwellian EEDF. However, electron-electron collisions are there to refill this tail. As such, they directly influence the excitation frequency. Therefore, assuming a Maxwellian EEDF results in overestimating the excitation frequency and thereby the population of excited states. However, recall that in our model, there are two main population mechanisms of the excited levels, electron impact on ground state atoms and dissociative recombination. As discussed in Sec. II D 1, the population of the 4*s* block of excited states is mainly determined by the dissociative recombination, which is controlled by the radial distribution of the gas temperature. Therefore, taking into account the effect of electron-electron collisions on the EEDF in our model should only slightly influence the radial contraction of the discharge.

V. CONCLUSION

We have developed a model for atmospheric-pressure plasmas in the electron density range over which radial contraction of the plasma column can be observed, namely, 10^{12}–10^{15} cm^{-3}. At densities higher than 10^{15} cm^{-3}, the contraction phenomenon tends to disappear. Contraction in rare-gas discharges was shown to be related to the presence of molecular ions, the concentration of which is determined by the local value of the gas temperature. Therefore, we conclude that contraction is due to nonuniform gas heating.

An important feature accounted for by the model is the influence exerted on discharge contraction by the radial nonuniformity of the electric field intensity. The more nonuniform is the electric field intensity, the less contracted is the discharge (at least until filamentation occurs). This is why microwave-sustained discharges are less contracted than dc discharges, given the same power density level.

The model was compared with experimental data obtained with surface-wave-sustained discharges, showing a good agreement on many aspects of discharge contraction.

ACKNOWLEDGMENTS

This work was financed by the Fonds de Recherche sur la Nature et les Technologies (FRNTQ) of the Gouvernement du Québec and by the Conseil de Recherches en Sciences Naturelles et en Génie (CRSNG) of Canada.

APPENDIX: EXPRESSIONS FOR THE RATE COEFFICIENTS OF THE COLLISIONAL AND TRANSPORT PROCESSES INVOLVED IN THE MODELING OF THE ARGON DISCHARGE

The frequency for direct ionization [Eqs. (5) and (7)] is [31]

$$\nu_i = \alpha_{0i} N = 1.27 \times 10^{-8} \sqrt{T_e\ (\mathrm{eV})} \exp\{-[U_i\ (\mathrm{eV})]/[T_e\ (\mathrm{eV})]\} \times [N\ (\mathrm{cm}^{-3})], \tag{A1}$$

where α_{0i} is the rate constant for direct ionization and $U_i = 15.76$ eV is the ionization energy of the argon atom.

The process of step ionization requires the density of the 4*s* excited states, which is determined by the steady-state balance equation of the 4*s* block:

$$\Delta(D_j N_j) + \alpha_{0j} n_e N + \rho_{dr} n_e n_{i2} - \alpha_{j0} n_e N_j - \alpha_{ji} n_e N_j = 0. \tag{A2}$$

The 4*s* block (Fig. 1) is populated by electron collisions on the ground state atom (with rate coefficient α_{0j}) and by dissociative recombination (with rate coefficient ρ_{dr}). Depopulation of the 4*s* block occurs through diffusion (with coefficient D_j), through electron-collision deexcitation to the ground state (with the coefficient α_{j0}), and through ionization (with rate coefficient α_{ji}). Then, Eq. (A2) yields the density of the 4*s* block as

$$N_j = \frac{\alpha_{0j} n_e N \tau_j + \rho_{dr} n_{i2} n_e \tau_j}{1 + (\alpha_{j0} + \alpha_{ji}) n_e \tau_j}, \tag{A3}$$

where $\tau_j = \Lambda_j^2 / D_j$ is the diffusion time with characteristic length $\Lambda_j = R/2.4$ and diffusion coefficient $D_j\ (\mathrm{cm}^2/\mathrm{s}) = 1.0 \times 10^{17} \sqrt{T_g\ (\mathrm{K})}/[N\ (\mathrm{cm}^{-3})]$ [38]. Using Eq. (A3), the step-ionization rate entering Eqs. (5) and (7) can be expressed in the form

$$\nu_{si} n_e = \alpha_{ji} n_e N_j = \frac{\rho_{si} n_e^2 + \rho_{rk} n_{i2} n_e^2}{1 + \eta n_e}, \tag{A4}$$

where

$$\rho_{si}\ (\mathrm{cm}^3/\mathrm{s}) = \alpha_{0j} \alpha_{ji} N \tau_j = 1.14 \times 10^{-33} \frac{[N^2\ (\mathrm{cm}^{-3})][R^2(\mathrm{cm})][T_e\ (\mathrm{eV})]}{\sqrt{T_g}\ (\mathrm{K})} \times \exp\left(-\frac{U_i\ (\mathrm{eV})}{T_e\ (\mathrm{eV})}\right) \tag{A5}$$

is the rate coefficient for the step ionization due to the population of the 4*s* block from the ground state and

$$\rho_{rk}\ (\mathrm{cm}^6/\mathrm{s}) = \rho_{dr} \alpha_{ji} \tau_j \tag{A6}$$

is the rate coefficient for step ionization accounting for the population of the 4*s* block due to dissociative recombination where $\alpha_{ji} = 1.37 \times 10^{-7} \sqrt{T_e\ (\mathrm{eV})} \exp[-(U_i - U_j)/T_e]$ is the rate coefficient for ionization from the 4*s* block [31] and

$$\eta\ (\mathrm{cm}^3) = (\alpha_{j0} + \alpha_{ji}) \tau_j \cong 2.38 \times 10^{-25} \frac{[N\ (\mathrm{cm}^{-3})][R^2\ (\mathrm{cm})] \sqrt{T_e\ (\mathrm{eV})}}{\sqrt{T_g\ (\mathrm{K})}} \times \exp\left(-\frac{[U_i\ (\mathrm{eV})] - [U_j\ (\mathrm{eV})]}{T_e\ (\mathrm{eV})}\right) \tag{A7}$$

is the coefficient accounting for the saturation of the various step-ionization processes.

The rate coefficient for dissociative recombination is [39]

$$\rho_{dr}\ (\mathrm{cm}^3/\mathrm{s}) = 1.04 \times 10^{-6} \left(\frac{T_e\ (\mathrm{K})}{300}\right)^{-0.67} \times \frac{\{1 - \exp(-418/[T_g\ (\mathrm{K})]\}}{\{1 - 0.31 \exp(-418/[T_g\ (\mathrm{K})]\}}, \tag{A8}$$

and the rate coefficient for the three-body recombination reads [28]

$$\rho_{tr}\ (\mathrm{cm}^6/\mathrm{s}) = 8.75 \times 10^{-27} [T_e\ (\mathrm{eV})]^{-9/2}. \tag{A9}$$

The rate coefficient for the conversion of atomic ions into molecular ions is [40]

$$k_1\ (\mathrm{cm}^6/\mathrm{s}) = 2.25 \times 10^{-31} \{[T_g\ (\mathrm{K})]/300\}^{-0.4}. \tag{A10}$$

The rate coefficients for the dissociation of molecular ions by electron and by atom impacts are in the same form as given in Ref. [29]. They are, respectively,

$$k_2\ (\mathrm{cm}^3/\mathrm{s}) = 1.11 \times 10^{-6} \exp\left[-\frac{2.94 - 3\{[T_g\ (\mathrm{eV})] - 0.026\}}{T_e\ (\mathrm{eV})}\right] \tag{A11}$$

and

$$k_3\ (\mathrm{cm^3/s}) = \frac{5.22\times10^{-10}}{T_g\ (\mathrm{eV})}\exp\left(-\frac{1.304}{T_g\ (\mathrm{eV})}\right). \quad \text{(A12)}$$

In Eqs. (1), (3), (10), (12), and (13), the elastic collision frequency is the sum of the frequencies for electron-neutral and electron-ion elastic collisions, i.e., $\nu=\nu_{ea}+\nu_{ei}$. The frequency of electron-neutral elastic collisions for argon is [41]

$$\nu_{ea}\ (\mathrm{s^{-1}}) = 1.84\times10^{-8}[T_e^{3/2}\ (\mathrm{eV})][N\ (\mathrm{cm^{-3}})], \quad \text{(A13)}$$

while the frequency for electron-ion elastic collisions [42] is

$$\nu_{ei}\ (\mathrm{s^{-1}}) \cong \frac{4.8[n_e\ (\mathrm{cm^{-3}})]}{T_e^{3/2}\ (\mathrm{K})}\ln\left(\frac{T_e^{3/2}\ (\mathrm{K})}{1.21\times10^{-4}\sqrt{n_e\ (\mathrm{cm^{-3}})}}\right). \quad \text{(A14)}$$

The total excitation frequency entering Eq. (3) is [41]

$$\nu_* = 1.04\times10^{-8}\sqrt{T_e\ (\mathrm{eV})}\exp \times\{-[U_*\ (\mathrm{eV})]/[T_e\ (\mathrm{eV})]\}\times[N\ (\mathrm{cm^{-3}})], \quad \text{(A15)}$$

where $U_*=11.548$ eV for argon.

The transport coefficients for energy and particles are as follows. The gas thermal conductivity [Eq. (1)] is obtained from Ref. [43]. In the temperature range $T_g=300$–6000 K, its coefficient can be expressed as

$$\chi_g\ (\mathrm{W/mK}) = 3.5\times10^{-4}[T_g^{0.68}\ (\mathrm{K})]. \quad \text{(A16)}$$

The electron thermal conductivity [Eq. (3)] is obtained from the electron diffusion coefficient D_e and it reads

$$\chi_e\ (\mathrm{W/mK}) = \frac{5}{2}n_eD_e. \quad \text{(A17)}$$

The data for the mobility of argon atomic ions b_{i1} and argon molecular ions b_{i2} were taken from Ref. [44].

[1] C. Kenty, Phys. Rev. **126**, 1235 (1962).
[2] J. T. Massey and S. M. Cannon, J. Appl. Phys. **36**, 361 (1965).
[3] J. T. Massey, J. Appl. Phys. **36**, 373 (1965).
[4] V. Yu. Baranov and K. N. Ul'yanov, Zh. Tekh. Fiz. **39**, 249 (1969) [Sov. Phys. Tech. Phys. **14**, 176 (1969)]; **39**, 259 (1969) [**14**, 183 (1969)].
[5] Yu. B. Golubovskii and R. Sonneburg, Zh. Tekh. Fiz. **49**, 295 (1979) [Sov. Phys. Tech. Phys. **24**, 173 (1979)].
[6] D. B. Ogle and G. A. Woolsey, J. Phys. D **20**, 453 (1987).
[7] E. I. Toader, J. Phys. D **28**, 75 (1995).
[8] N. Djermanova, D. Grozev, K. Kirov, K. Makasheva, A. Shivarova, and Ts. Tsvetkov, J. Appl. Phys. **86**, 738 (1999).
[9] Y. Kabouzi, M. D. Calzada, M. Moisan, K. C. Tran, and C. Trassy, J. Appl. Phys. **91**, 1008 (2002).
[10] E. Castaños Martinez, Y. Kabouzi, K. Makasheva, M. D. Calzada, M. Moisan, and C. Trassy, in Proceedings of the 14th International Colloquium on Plasma Processes (CIP 2003), Antibes, France, 2003 (unpublished).
[11] A. V. Eletskii and B. M. Smirnov, Zh. Tekh. Fiz. **40**, 1682 (1970) [Sov. Phys. Tech. Phys. **15**, 1308 (1971)].
[12] G. L. Rogoff, Phys. Fluids **15**, 1931 (1972).
[13] P. K. Milsom, J. Phys. D **29**, 403 (1996).
[14] K. N. Ul'yanov, Zh. Tekh. Fiz. **43**, 570 (1973) [Sov. Phys. Tech. Phys. **18**, 360 (1973)].
[15] V. L. Bychkov and A. V. Eletskii, Fiz. Plazmy **4**, 942 (1978) [Sov. J. Plasma Phys. **4**, 528 (1978)].
[16] Yu. B. Golubovskii and R. Sonneburg, Zh. Tekh. Fiz. **49**, 302 (1979) [Sov. Phys. Tech. Phys. **24**, 177 (1979)].
[17] G. M. Petrov and C. M. Ferreira, Phys. Rev. E **59**, 3571 (1999).
[18] Yu. B. Golubovskii, H. Lange, V. A. Maiorov, I. A. Porokhova, and V. P. Sushkov, J. Phys. D **36**, 694 (2003).
[19] U. Kortshagen, H. Schlüter, and A. V. Maximov, Phys. Scr. **46**, 450 (1992).
[20] M. Moisan and J. Pelletier, *Microwave Excited Plasmas* (Elsevier, New York, 1992).
[21] Z. Zakrzewski, J. Phys. D **16**, 171 (1983).
[22] M. Moisan, J. Hubert, and R. Pantel, Contrib. Plasma Phys. **30**, 293 (1990).
[23] M. Moisan and Z. Zakrzewski, Plasma Sources Sci. Technol. **4**, 379 (1995).
[24] Yu. M. Aliev, H. Schlüter, and A. Shivarova, *Guided-Wave-Produced Plasmas* (Springer, Berlin, 2000).
[25] H. Nowakowska, Z. Zakrzewski, M. Moisan, and M. Lubański, J. Phys. D **31**, 1422 (1998).
[26] V. M. Lelevkin, D. K. Otorbaev, and D. C. Schram, *Physics of Non-Equilibrium Plasmas* (North-Holland, Amsterdam, 1992).
[27] L. M. Biberman, V. S. Vorob'ev, and I. T. Yakubov, *Kinetics of Non-Equilibrium Low-Temperature Plasma* (Plenum, New York, 1987).
[28] Yu. P. Raizer, *Gas Discharges* (Springer, Berlin, 1991).
[29] J. Jonkers, M. van de Sande, A. Sola, A. Gamero, A. Rodero, and J. van der Mullen, Plasma Sources Sci. Technol. **12**, 464 (2003).
[30] V. E. Golant, P. Zhilinsky, and I. E. Sakharov, *Fundamentals of Plasma Physics* (Wiley, New York, 1977).
[31] K. Makasheva and A. Shivarova, Phys. Plasmas **8**, 836 (2001).
[32] J. Berndt, K. Makasheva, H. Schlüter, and A. Shivarova, Plasma Sources Sci. Technol. **11**, 208 (2002).
[33] This is due mainly to the increase of the gas temperature which increases the diffusion time τ_j of the 4*s* block of excited atoms, which appears in the rate coefficient ρ_{rk}.
[34] M. Zethoff and U. Kortshagen, J. Phys. D **25**, 1574 (1992).
[35] J. Berndt, D. Grozev, and H. Schlüter, J. Phys. D **33**, 877 (2000).
[36] St. Lishev, L. Marinova, H. Schlüter, and A. Shivarova, Vacuum **69**, 153 (2003).
[37] A. V. Maximov and H. Schlüter, Phys. Scr. **65**, 263 (2002).
[38] A. V. Phelps and J. P. Molnar, Phys. Rev. **89**, 1202 (1953).
[39] A. J. Cunningham, T. F. O'Malley, and R. M. Hobson, J. Phys. B **14**, 773 (1981).
[40] J. D. C. Jones, D. J. Lister, D. P. Wareing, and N. D. Twiddy, J. Phys. B **13**, 3247 (1980).
[41] U. Kortshagen, A. Shivarova, E. Tatarova, and D. Zamfirov, J.

Phys. D **27**, 301 (1994).
[42] J. P. Delcroix and A. Bers, *Physique des Plasmas* (InterEditions, Paris, 1994).
[43] B. Pateyron, M. F. Elshinger, G. Delluc, and J. Auberton, *ADEP—Banque des données de l'Université et du CNRS* (Direction des Bibliothèques des Musées et de l'Information Scientifique et Technique, Paris, 1986).
[44] E. W. McDaniel and E. A. Mason, *The Mobility and Diffusion of Ions in Gases* (Wiley, New York, 1973).